

Received 12 January 2024

Accepted 23 February 2024

Edited by F. Maia, Uppsala University, Sweden

Keywords: droplet microfluidics; crystal miniaturization; micromixing; time-resolved serial crystallography.

PDB references: lysozyme control, 8s2u; lysozyme droplet, 8s2v; Pdx1 control, 8s2w; Pdx1 droplet, 8s2x

Supporting information: this article has supporting information at www.iucrj.org

Droplet microfluidics for time-resolved serial crystallography

Jack Stubbs,^{a,b,*} Theo Hornsey,^a Niall Hanrahan,^{c,d} Luis Blay Esteban,^e Rachel Bolton,^{a,b} Martin Malý,^{a,d} Shibom Basu,^f Julien Orlans,^g Daniele de Sanctis,^g Jung-uk Shim,^h Patrick D. Shaw Stewart,ⁱ Allen M. Orville,^{b,j} Ivo Tews^{a,d} and Jonathan West^{d,k,*}

^aSchool of Biological Sciences, Faculty of Environmental and Life Sciences, University of Southampton, Southampton SO17 1BJ, United Kingdom, ^bDiamond Light Source, Harwell Science and Innovation Campus, Didcot, Oxfordshire OX11 0DE, United Kingdom, ^cSchool of Chemistry, Faculty of Engineering and Physical Sciences, University of Southampton, Southampton SO17 1BJ, United Kingdom, ^dInstitute for Life Sciences, University of Southampton, Southampton SO17 1BJ, United Kingdom, ^eUniversitat Carlemany, Avenida Verge de Canolich, 47, Sant Julia de Loria, Principat d'Andorra AD600, Spain, ^fEuropean Molecular Biology Laboratory, Grenoble Outstation, 71 Avenue des Martyrs, CS 90181, Grenoble 38042, Cedex 9, France, ^gEuropean Synchrotron Radiation Facility (ESRF), 71 Avenue des Martyrs, Grenoble 38042, Cedex 9, France, ^hFaculty of Engineering and Physical Sciences, University of Leeds, Leeds LS2 9JT, United Kingdom, ⁱDouglas Instruments Ltd, East Garston, Hungerford RG17 7HD, United Kingdom, ^jResearch Complex at Harwell, Harwell Science and Innovation Campus, Didcot, Oxfordshire OX11 0FA, United Kingdom, and ^kCancer Sciences, Faculty of Medicine, University of Southampton, Southampton SO17 1BJ, United Kingdom. *Correspondence e-mail: jrs1u21@soton.ac.uk, j.j.west@soton.ac.uk

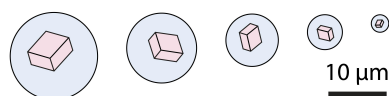
Serial crystallography requires large numbers of microcrystals and robust strategies to rapidly apply substrates to initiate reactions in time-resolved studies. Here, we report the use of droplet miniaturization for the controlled production of uniform crystals, providing an avenue for controlled substrate addition and synchronous reaction initiation. The approach was evaluated using two enzymatic systems, yielding 3 µm crystals of lysozyme and 2 µm crystals of Pdx1, an *Arabidopsis* enzyme involved in vitamin B6 biosynthesis. A seeding strategy was used to overcome the improbability of Pdx1 nucleation occurring with diminishing droplet volumes. Convection within droplets was exploited for rapid crystal mixing with ligands. Mixing times of <2 ms were achieved. Droplet microfluidics for crystal size engineering and rapid micromixing can be utilized to advance time-resolved serial crystallography.

1. Introduction

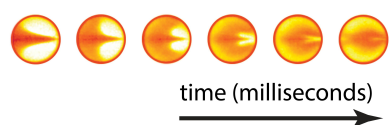
Modern crystallography incorporates diffraction data collection at room temperature, providing a means to emulate physiological conditions whilst also observing the dynamic nature of proteins (Orville, 2020; Fraser *et al.*, 2011; Fischer, 2021). Challenges posed by elevated radiation damage (Holton, 2009; Garman, 2010; Garman & Weik, 2023) can be overcome by the collection of multiple datasets or the application of serial methods. No longer can optimal crystals be hand-picked, but instead large numbers of uniform microcrystals must be prepared. Advancements in instrumentation, including high-flux synchrotron sources and extreme-brilliance X-ray free-electron lasers (XFELs) (Chapman *et al.*, 2011; Chapman, 2019; Barends *et al.*, 2022), coupled with developments in automation, data processing, detector technologies (Förster *et al.*, 2019) and sample delivery, will ensure time-resolved experiments using serial methods will become routine in the near future.

Crystal size is a critical parameter for many reasons (Shoeman *et al.*, 2022); it should be tuned to the synchrotron or XFEL beam size [$\sim 1\text{--}20\text{ }\mu\text{m}$ (Evans *et al.*, 2011)] for

Crystal Scaling



Micromixing



OPEN ACCESS

Published under a CC BY 4.0 licence

improved signal-to-noise ratio in the X-ray diffraction pattern and efficient use of the protein sample. For time-resolved studies, the key advantages of small crystals are short substrate transport paths into the crystal lattice for rapid reaction triggering or short light paths for full penetration of exciting light. For illustration, substrate transport into the centre of a 2 µm crystal (*i.e.* 1 µm travel) is dependent on size (Schmidt, 2013) and several other factors, including the ligand diffusion coefficient, initial concentration, charge, mother liquor viscosity and crystal lattice packing, with time scales ranging from 400 µs for O₂ (32 Da) to 3.5 ms for larger ligands (*e.g.* ceftriaxone, 554 Da). Crystal uniformity is critically important, especially for synchronized reaction triggering, but also to avoid large crystals clogging capillaries used in many sample delivery systems. Ideal results will derive from monodisperse microcrystal slurries, robust sample delivery methods and reaction initiation strategies that exploit particular X-ray source characteristics and limit sample consumption.

Preparing large numbers of uniformly small crystals is an on-going challenge for the field. Although microcrystal showers are often the first hit in sparse matrix vapour diffusion screens, they typically need to be scaled-up by batch methods to produce the volumes required for serial crystallography experiments; this may reach millilitre volumes for time-course experiments with multiple time-point datasets (Tenboer *et al.*, 2014; Beale *et al.*, 2019; Stohrer *et al.*, 2021; Beale & Marsh, 2021; Shoeman *et al.*, 2022).

Crystal formation typically comprises a nucleation phase, followed by a growth phase. Under some crystallization conditions, nucleation occurs rapidly and, as crystals grow, they deplete protein in solution, and thereby prevent further nucleation. A popular strategy is to fragment crystals to make seeds to control crystal growth. Seeds effectively bypass nucleation, acting as nuclei to instantly initiate growth such that protein is shared throughout crystal growth (Stura & Wilson, 1990; D'Arcy *et al.*, 2007; Shaw Stewart *et al.*, 2011; Shoeman *et al.*, 2022). Nevertheless, this still results in crystal size variation, for example, if two seeds are in close proximity the competition for protein will result in a pair of smaller than average crystals. New approaches are therefore needed to compartmentalize single-crystal growth and produce uniformly sized crystals.

Microfluidics has attracted significant attention for crystallography as it can precisely control reaction environments (Li & Ismagilov, 2010; Puigmartí-Luis, 2014; Shi *et al.*, 2017; Sui & Perry, 2017). Initial efforts involved nanolitre environments enabling counter-diffusion for exploring phase diagrams (Hansen *et al.*, 2002; Zheng *et al.*, 2004; Li & Ismagilov, 2010), or dialysis to decouple and optimize nucleation separately from growth (Shim *et al.*, 2007a,b; Selimović *et al.*, 2009). Droplet microfluidic formats then allowed better control of crystal formation by negative feedback through protein depletion during crystal growth (Dombrowski *et al.*, 2007; Heymann *et al.*, 2014), defining crystal size by the available protein, *i.e.* droplet volume. Droplet microfluidic crystallizations have been demonstrated for lysozyme, glucose isomerase, trypsin, concanavalin A, D1D2 spliceosomal

snRNP particles (Heymann *et al.*, 2014; Akella *et al.*, 2014), sugar hydrolase and sialate O-acetyltransferase (Babnigg *et al.*, 2022). Importantly, microfluidic droplets are highly monodisperse, which allows the protein supply to be exactly metered to achieve crystal uniformity. Studies to date have optimized droplet size to achieve single-crystal occupancy for the formation of large crystals suitable for obtaining synchrotron diffraction data *in situ*.

For time-resolved experiments there is also the challenge of rapidly triggering reactions with substrates and ligands (Echelmeier *et al.*, 2019). Mix-and-inject methods that first emerged (Weierstall *et al.*, 2012; Calvey *et al.*, 2016; Stagno *et al.*, 2017; Olmos *et al.*, 2018; Ishigami *et al.*, 2019; Dasgupta *et al.*, 2019; Pandey *et al.*, 2021; Murakawa *et al.*, 2022) involved coaxial flows with a core crystal stream. Hydrodynamic focusing results in stream-thinning to provide short paths for the transport of substrate molecules into the crystal prior to high-velocity injection into the beam using a gas dynamic virtual nozzle (GDVN) (DePonte *et al.*, 2008). As an efficient, high-hit-rate alternative, piezoelectric or acoustic drop-on-demand methods are gaining popularity for the delivery of substrate droplets onto crystals presented on fixed targets (Mehrabani *et al.*, 2019) or tape drives (Roessler *et al.*, 2016; Fuller *et al.*, 2017; Butryn *et al.*, 2021). Here, picolitre substrate volumes are dispensed onto individual crystals or crystals contained in nanolitre droplets (both within a humidified environment). Mixing initially occurs by impact-induced convection, followed by diffusion, then the registration of the crystal into the beam after a defined time delay (2 ms and upwards). These sample delivery methods and their considerations are captured in recent reviews (Schulz *et al.*, 2022; Barends *et al.*, 2022).

In this contribution, we explore droplet scaling from nanolitre volumes down to sub-picolitre volumes and demonstrate the ability to engineer crystal size and uniformity. Using *Arabidopsis thaliana* Pdx1, an enzyme involved in vitamin B6 biosynthesis (Rodrigues *et al.*, 2017, 2022), and lysozyme, we demonstrate crystal scaling to suitable dimensions and numbers for time-resolved serial crystallography. We show that with diminishing volumes, nucleation becomes improbable, but this can be countered by seeding. We go on to exploit droplets as convective environments for rapid micro-mixing, achieving mixing within 2 ms to support future strategies for understanding structural dynamics with high temporal resolution.

2. Material and methods

2.1. Protein expression, purification and crystallization

2.1.1. Lysozyme. Lysozyme (chicken egg white, Melford) was batch-crystallized using a ratio of one part 20 mg ml⁻¹ lysozyme in 20 mM sodium acetate, pH 4.6 to four parts of mother liquor; 6% (w/v) PEG 6000 in 3.4 M NaCl and 1 M sodium acetate, pH 3.0; [adapted from previous conditions (Martin-Garcia *et al.*, 2017)]. The mixture was vortexed for 5 s and left to crystallize for 1 h at room temperature.

2.1.2. Trypsin. Trypsin (bovine pancreas, type I, Merck) needles were crystallized using seeded vapour diffusion conditions as previously described (Heymann *et al.*, 2014). Seed stocks were prepared by pooling crystals from many vapour diffusion drops, dilution in mother liquor [11–14% (w/v) PEG 4000, 15% ethylene glycol, 200 mM SiSO₄, 100 mM MES, pH 6.5] and vortexing with a Hampton Seed Bead for 180 s by alternating between 30 s of vortexing and 30 s on ice followed by storage at −20°C. Seeded-batch trypsin crystallization involved one part 65 mg ml^{−1} trypsin in 3 mM CaCl₂ with benzamidine, one part mother liquor and one part seed prepared in mother liquor. The mixture was vortexed for 5 s and incubated at room temperature overnight.

2.1.3. Pdx1. Plasmid encoding wild-type Pdx1.3 (UniProt ID: Q8L940; EC: 4.3.3.6; Rodrigues *et al.*, 2017) was transformed into BL21 (DE3) competent *E. coli* cells, and grown to OD₆₀₀ 0.6 at 37°C. After induction with 25% (w/v) lactose and growth for a further 16 h at 30°C, cells were harvested by centrifugation. Cells were resuspended in lysis buffer [50 mM Tris pH 7.5, 500 mM sodium chloride, 10 mM imidazole, 2% (v/v) glycerol] and sonicated on ice. The lysate was ultracentrifuged at 140 000g at 4°C for 1 h, filtered and immobilized on a metal ion affinity chromatography HisTrap HP column (GE Healthcare). Pdx1 was washed and eluted with lysis buffer, containing 50 mM and 500 mM imidazole, respectively, as well as 5% (v/v) glycerol. The eluted protein was buffer-exchanged into gel filtration buffer (20 mM Tris pH 8.0, 200 mM KCl), before centrifugal concentration with a 30 kDa cut-off (Vivaspin 20, Sartorius). Crystals for preparing seeds were produced by combining (1:1) ~12 mg ml^{−1} Pdx1 with mother liquor (600 mM sodium citrate, 100 mM HEPES pH 7) as 10 µl vapour diffusion drops in 24-well XRL plates (Molecular Dimensions). Crystals for seed stocks grew overnight and varied in size from 10 to 50 µm in length. Vortexing with a Hampton Seed Bead was carried out for a total of 180 s by alternating between 30 s of vortexing and 30 s on ice followed by storage at −20°C. Batch crystallization involved a 1:1:1 mixture of 12 mg ml^{−1} Pdx1, seed (10⁵–10⁷ ml^{−1}) and mother liquor. In droplets a 2:1 mixture of seeds (10⁷ ml^{−1}) diluted in mother liquor with 12 mg ml^{−1} Pdx1 was used.

2.2. Droplet microfluidics

2.2.1. Device fabrication. Microfluidic devices (Whitesides, 2006) were replicated by soft lithography (Whitesides *et al.*, 2001) using SU-8 on silicon wafers. Fabrication protocols for the different SU-8 heights are described in the SU-8 2000 technical data sheet made available by Kayaku Advanced Materials. Poly(dimethylsiloxane) (PDMS, Sylgard 184) was cured on the SU-8 wafers at 60°C for 2 h, with the PDMS used to counter-mould polyurethane (Smooth-Cast 310) copies of the SU-8 wafers. Subsequent PDMS devices were cured in the polyurethane moulds for 2 h at 60°C. A range of different droplet microfluidic devices were used for the generation of nanolitre to femtolitre droplets. Droplet generation junction dimensions, flow rates and droplet characteristics for the different protein systems are documented in Tables S1–S3 (see

the CAD-file in the supporting information). Tubing ports were introduced using 1 mm-diameter Miltex biopsy punches (Williams Medical Supplies Ltd). Devices were bonded to glass microscope slides using a 30 s oxygen plasma treatment (Femto, Diener Electronic) followed by channel surface functionalization using 1% (v/v) trichloro(1*H*,1*H*,2*H*,2*H*-perfluorooctyl) silane (Merck) in HFE-7500 (3M Novec).

2.2.2. Microfluidic experimental setup. The experimental setup for droplet generation is shown in Fig. S1. The process involved the preparation of syringes containing protein, mother liquor and fluorinated oil (QX200, BioRad) which acts as the carrier phase. Pdx1 and trypsin I droplet preparations required the use of seeds within the mother liquor. Syringes were interfaced with 25 G needles (~1.7 µl dead volume) for connecting to the microfluidic ports via polythene tubing (ID = 0.38 mm, OD = 1.09 mm, Smiths Medical). Syringe pumps (Fusion 100, Chemyx) were used to deliver reagents for droplet generation. Droplet generation was monitored using a Phantom Miro310 (Ametek Vision Research) high-speed camera mounted on an inverted microscope (CKX41, Olympus). Droplets were collected in microcentrifuge tubes and stored at room temperature for 2–3 days with a mineral oil overlay to prevent coalescence. Droplet dimensions and crystal occupancy were measured using a supervised *ImageJ* (NIH) process. Lambda (λ) is used to denote the average number of crystals per droplet.

2.2.3. Crystal retrieval and analysis. Crystals were retrieved from droplets by a procedure called ‘breaking the emulsion’. First, the QX200 oil is removed, then a tenfold volume (relative to emulsion volume) of mother liquor is added. Next, a volume of 1*H*,1*H*,2*H*,2*H*-perfluoro-1-octanol (PFO, Merck) is added to the emulsion with gentle pipetting used to break the emulsion. The PFO exchanges with the commercial surfactant surrounding the droplets, allowing the aqueous compartments of droplets to contact each other and coalesce. Finally, the single aqueous volume containing the crystals is removed for analysis by mounting on a coverslip for oil immersion imaging with a 60×/1.4NA objective (Olympus). Crystal dimensions were measured using a custom MATLAB script (<https://github.com/luiblaes/Crystallography>) and manually validated.

2.3. Serial synchrotron crystallography

Lysozyme and Pdx1 crystals were concentrated by settling and applied to sheet-on-sheet (SOS) chips (Doak *et al.*, 2018). This involved removal of excess liquid and sandwiching 3–5 µl of the crystal slurry between two Mylar films and sealing inside a metal mount. A total of 81 800 images were collected per chip. Serial synchrotron crystallography (SSX) data for lysozyme and Pdx1 crystals grown in batch and within microfluidic droplets were collected on the new ID29 beamline at the European Synchrotron Radiation Facility (ESRF, France) using a 2 × 4 µm (*V* × *H*) beam of 11.56 keV X-rays, with a 90 µs pulse and 231.25 Hz repetition rate, and a 20 µm step movement between images. A JUNGFRU 4M detector (Mozzanica *et al.*, 2018) with a sample-to-detector distance of

175 mm (1.8 \AA in the corner) was used to collect diffraction patterns. Full information on data processing, structure determination and refinement are available in the supporting information.

2.4. Mixing in droplets and image analysis

Mixing of lysozyme crystals ($7 \times 2 \text{ }\mu\text{m}$; grown by batch crystallization) with 25 mM sulfanilic acid azochromotrop (SAA, Merck, $\lambda_{\text{max}} = 505\text{--}510 \text{ nm}$), a highly absorbing red dye, was investigated using $30 \times 40 \text{ }\mu\text{m}$ droplet-generation junctions with an oil:aqueous flow ratio of 2:1. The crystal:dye flow ratio was modulated along with total flow rates ranging from 7.5 to $45 \text{ }\mu\text{l min}^{-1}$. To retain crystals in suspension for ensuring continuous crystal delivery to the microfluidic device, we used automated syringe rotation (Lane *et al.*, 2019). In an alternative setup, a droplet generator producing SAA droplets was positioned upstream of an inlet for the introduction of pre-formed $\sim 70 \text{ }\mu\text{m}$ -diameter droplets containing lysozyme crystals. The lysozyme and SAA droplets were synchronized for one-to-one interception, followed by surfactant exchange with PFO for droplet fusion and ensuing circulation-driven micromixing. This experiment involved $12.5 \text{ }\mu\text{l min}^{-1}$ 10% (v/v) QX200 in HFE7500, $4 \text{ }\mu\text{l min}^{-1}$ lysozyme, $5 \text{ }\mu\text{l min}^{-1}$ SAA dye and $4 \text{ }\mu\text{l min}^{-1}$ PFO flow rates. For both strategies, diffusive-convective mixing of the SAA dye was captured by high-speed imaging (Phantom Miro310, Ametek Vision Research). Droplets were individually analysed to understand mixing with and without crystals. The coefficient of variation (CV) of the intensity of pixels defining each droplet was used as the mixing measure. CV approaches zero as the dye is homogenized throughout the droplet. The time from stream combination to a 5% pixel intensity CV value was used to define the mixing time. Mixing analysis was automated using a MATLAB script with 15 single droplet kymographs used to derive mixing time statistics.

3. Results

3.1. Experimental design

Droplet microfluidic designs incorporated aqueous inlets for protein, mother liquor, seed and another for the fluorinated oil with flow-focusing used for droplet generation [Fig. 1(a)]. Droplet generation junction dimensions were used to scale droplet volumes from ~ 750 to $\sim 1 \text{ pl}$ to investigate conditions for controlling lysozyme and Pdx1 crystal size and uniformity. To understand the effects of droplet confinement, the resulting crystals were compared with those grown under conventional batch conditions. Droplet microfluidics was then investigated as a means to rapidly mix crystals with substrates. Crystals were either encapsulated with substrate during droplet generation or crystal-containing droplets were fused with substrate-containing droplets.

3.2. Lysozyme crystallization in microfluidic droplets

Lysozyme is a well known standard that undergoes extremely fast nucleation (Forsythe *et al.*, 1999). Indeed, the

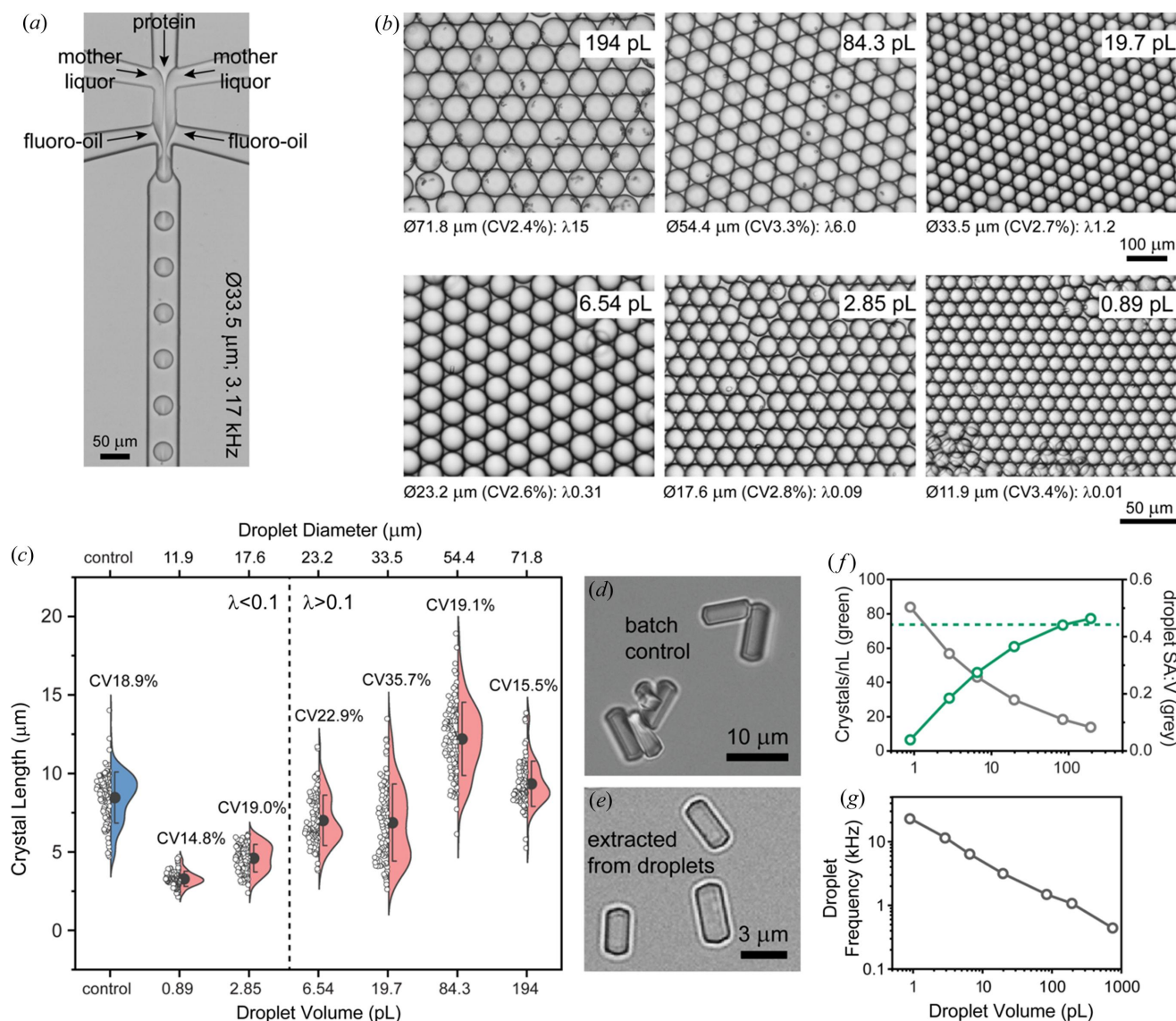
nucleation rate in our batch crystallization method is too fast to measure (Video S1 of the supporting information), but a resultant crystal density of $\sim 80 \text{ nl}^{-1}$ was observed ($\sim 80 \text{ M ml}^{-1}$). The rapid growth of lysozyme crystals introduces negative feedback to prevent later nucleation events. This aids length uniformity, producing crystals with an $8 \text{ }\mu\text{m}$ average length and $\text{CV} \simeq 19\%$ [Fig. 1(c)].

Using batch crystallization as a benchmark we then sought to understand the effects of volume scaling by droplet confinement. Droplet microfluidics produced monodisperse ($\text{CV} < 4\%$) droplets ranging in size from 754 to 0.89 pl and crystal sizes ranging from 20 to $2 \text{ }\mu\text{m}$ [Figs. 1(a) and 1(b)]. In the largest droplets [754 pl ($\phi 113 \text{ }\mu\text{m}$)], crystals were too numerous to count, whereas smaller droplets showed a crystal occupancy ranging from an average of 15 crystals per droplet ($\lambda 15$) in 194 pl droplets to stochastically loaded 0.89 pl droplets with ~ 0.01 crystals per droplet ($\sim \lambda 0.01$) [Fig. 1(c)]. Multiple nucleation events within each droplet result in a high crystal size CV. As droplets are miniaturized, the mean occupancy falls below $\lambda 0.1$, giving rise to the majority of occupied droplets containing a single crystal. Confirming our expectations, single-crystal occupancy promotes uniformity, producing a crystal size CV of $\sim 15\%$ in 0.89 pl droplets. Importantly, single occupancy coupled with droplet volume control also confers crystal miniaturization, producing $\sim 3 \text{ }\mu\text{m}$ long lysozyme crystals in the smallest 0.89 pl droplets [Fig. 1(c)].

Attaining single-crystal occupancy while aiming to reduce crystal size by limiting droplet volume becomes inefficient as a consequence of the nucleation density. Beyond this, other losses are apparent with droplet miniaturization [Fig. 1(f)], with the crystal density falling from $\sim 80 \text{ crystals nl}^{-1}$ for batch controls and 194 pl droplets to $\sim 7 \text{ crystals nl}^{-1}$ in the 0.89 pl droplets. Losses correlate with the increased surface area to volume ratio associated with droplet miniaturization [Fig. 1(f)], which may implicate the surfactant droplet interface as an inhibitory environment for crystal formation. In terms of throughput, losses are compensated by droplet generation frequency increasing with droplet miniaturization. In practice, droplet generation frequency increases 50-fold from 0.44 kHz with the 754 pl droplets to 23.5 kHz with the 0.89 pl droplets [Fig. 1(g)]. Such throughput with incubation off-chip allows the mass production of crystals which would otherwise be greatly limited by device size when undertaking on-chip crystallization.

3.3. Pdx1 crystallization in microfluidic droplets with seeding

We next sought to investigate whether the droplet approach could be applied to a protein with more typical crystallization behaviour than lysozyme. We used Pdx1, where nucleation rates are much lower, resulting in only a few crystals, which is inadequate for populating small droplets with crystals. To address this issue, we prepared Pdx1 seeds to substantially increase the crystal density and synchronize crystal growth initiation.

**Figure 1**

Lysozyme crystal size control by droplet volume scaling. (a) Protein crystallization droplets generated at kilohertz frequencies by combining streams of lysozyme, mother liquor and fluorinated oil. (b) Using different devices and flow rates (see Table S1 of the supporting information), monodisperse droplets ($\text{CV} < 4\%$) can be produced with picolitre to femtolitre volumes. (c) Lysozyme crystals produced under batch conditions (control, blue) were on average $8 \mu\text{m}$ long. The length of lysozyme crystals produced in droplets (salmon) correlates with the droplet volume, with $\sim 3 \mu\text{m}$ -long crystals produced in the smallest 0.89 pL droplets. Crystal uniformity emerges when the average number of crystals per droplet (λ) is ≤ 0.1 . (d) and (e) Visual comparison of lysozyme crystals prepared in batch (control) and extracted from 0.89 pL droplets by breaking the emulsion. (f) Droplet volume miniaturization is associated with reduced crystal density normalized to crystals per nanolitre (green) which correlates with increasing the surface area to volume (SA:V, grey) ratio. The batch crystal density value is denoted by the green dashed line. (g) Gains in droplet generation frequency scale with droplet volume reduction.

Under batch conditions, the addition of seeds produced a crystal density of 10^7 ml^{-1} with an average length of $\sim 11 \mu\text{m}$ [Fig. 2(a)]. Accordingly, tenfold seed dilution in mother liquor reduced the number of crystals while providing more protein per crystal, resulting in $\sim 18 \mu\text{m}$ -long crystals for 1/10 seed dilutions and $30 \mu\text{m}$ -long-crystals for 1/100 seed dilutions [Fig. 2(a)]. In principle, seeding initiates crystal growth at the same time, providing equal access to protein throughout growth which results in same-sized crystals. In practice, crystals were variable in size, with a $\sim 25\%$ CV across the dilution series [Fig. 2(a)].

Translating the seeded crystallization of Pdx1 under batch conditions to droplet environments using 10^7 ml^{-1} seeds typically resulted in single-crystal occupancy to favour crystal length uniformity ($\text{CV} 7\text{--}16\%$) across a 200-fold range of droplet volumes ($1.1\text{--}219 \text{ pL}$) [Figs. 2(b) and 2(c)]. Droplet volume scaling with single-crystal occupancy allows the crystal size to be controlled, from $\sim 2 \mu\text{m}$ in length for the smallest 1.1 pL droplets, to $\sim 20 \mu\text{m}$ in length for the largest 219 pL droplets [Fig. 2(c)]. Overall, crystal size can be engineered by droplet volume while retaining uniformity, albeit with crystal occupancy decreasing with diminishing droplet volumes.

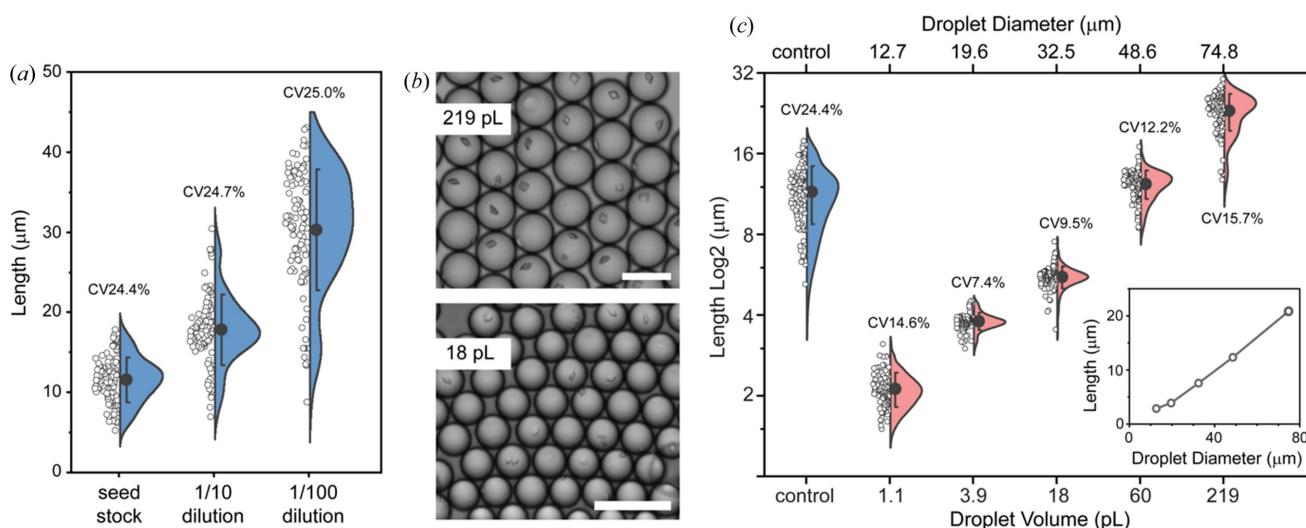


Figure 2

The effect of seeding under batch conditions compared with droplet conditions on Pdx1 crystal size. (a) Seeded batch Pdx1 crystallization involved a 1:1:1 mixture of Pdx1, seed (10^5 – 10^7 ml $^{-1}$) and mother liquor. The seed dilution affects crystal size (blue), but not crystal uniformity. (b) Pdx1 crystals were grown in droplets using a 2:1 mixture of seeds (10^7 ml $^{-1}$) in mother liquor with Pdx1. Pdx1 crystals grown in 219 and 18 pL monodisperse droplets typically have single occupancy (scale bars 100 μm). (c) Droplet miniaturization over a 200-fold range was used to control Pdx1 crystal length from ~20 to ~2 μm (salmon), with crystal length being proportional to droplet volume. (c, inset) Linear scaling of the crystal length with droplet diameter. Droplet confinement enables crystal-size uniformity (CVs 7.4–15.7%). Pdx1 crystals prepared in batch (control, blue) are large with low uniformity (CV 24.4%).

3.4. Considerations for crystallization in microfluidic droplets

3.4.1. Aspect ratio. The general applicability of droplets as environments for preparing a variety of different protein crystals is supported by previous work (Heymann *et al.*, 2014; Akella *et al.*, 2014; Babnigg *et al.*, 2022). To extend applicability, we sought to investigate the effect of droplet confinement on the growth of crystal needles. Using trypsin type I as a model needle system, it was evident that droplet diameters are insufficient to allow full elongation, resulting in a lower crystal axial ratio (l/w) or fragmentation into multiple small-needle crystals [Figs. S4(a) and S4(b)]. A similar effect is evident with parallelepiped-shaped lysozyme crystals, with the crystal axial ratio decreasing with droplet diameter [Fig. S4(c)]. This indicates that protein inclusion within the ends of elongated crystals is impeded within droplets.

3.4.2. Viscosity. Another consideration for the broader utility of droplet microfluidics for crystal preparation is the use of different crystallization mixtures. Precipitating agents such as poly(ethylene glycol) increase viscosity, which impacts the feasibility of producing stable droplet flows at sufficient throughput. To evaluate this effect, we prepared PEG 6000 solutions [0–25% (w/v)] ranging in viscosity from 1 to 21 mPa s and used these to observe the effect of viscosity on the generation of 50 μm-diameter droplets. Only an approximately threefold reduction in throughput was observed over these extremes (Fig. S5), indicating scope to apply droplet microfluidics to other crystallization conditions.

3.4.3. Minimum crystal size. The minimum crystal size is another consideration. Given that diffraction data can be obtained from sub-micrometre crystals (Gati *et al.*, 2017; Bückner *et al.*, 2020; Williamson *et al.*, 2023), and the 2–3 μm-long lysozyme and Pdx1 crystals prepared in ~1 pL droplets,

there is scope to further reduce droplet volumes. Though it is feasible to prepare monodisperse 5.4 μm-diameter droplets with a volume of 82 fl, the effect of greatly reduced seed occupancy and lower crystal formation frequency [Fig. 1(f)] prevented observable crystal formation [Fig. S6].

Smaller crystals are also harder to hit with a microfocus X-ray beam and impact sample delivery choice. For instance, small crystals will pass through 7 μm and larger apertures on fixed targets (Hunter *et al.*, 2014; Roedig *et al.*, 2015; Owen *et al.*, 2017; Mehrabi *et al.*, 2020), although smaller apertures are now emerging (Carrillo *et al.*, 2023). As an alternative, wells within fixed targets can be loaded by depositing 10–100s of picolitre droplets containing microcrystals using a piezo-electric injector. These droplets are larger than the aperture and held by surface tension to the well walls during data collection (Davy *et al.*, 2019).

3.5. Serial synchrotron crystallography

We tested the visually similar crystals of lysozyme and Pdx1 prepared in batch and droplets for diffraction quality, determining and comparing structures for the two scenarios. Though droplets can be directly dispensed on silicon fixed targets (Babnigg *et al.*, 2022), we opted to remove the fluorinated oil and surfactant to ensure optimal signal to noise. This can be achieved by a procedure called ‘breaking the emulsion’ [see Methods, compare Fig. S2].

SSX experiments were performed at the new ID29 serial beamline at ESRF. Data collection took 10 min with minimal sample consumption (3–5 μl volumes) using the ESRF sheet-on-sheet (SOS) chip sample holder (Doak *et al.*, 2018). A full dataset was achieved from a single chip of lysozyme with a microcrystal concentration of 10^8 ml $^{-1}$. However, Pdx1 required three chips to obtain complete data, owing to the

Table 1
Data collection and refinement statistics for lysozyme and Pdx1 crystals grown under batch conditions and in droplets.
Values in parentheses are for the high-resolution shell. For all datasets, the wavelength was 1.07 Å and the average crystal length was ~15 µm.

	Lysozyme control	Lysozyme droplet	Pdx1 control	Pdx1 droplet
Data collection				
No. of collected images	81800	81800	245400	245400
No. of hits	34032	22815	20268	20827
Hit rate (%)	41.6	27.9	8.2	8.5
Indexed images (single lattice)	29954	22304	19325	20635
Indexing rate (%)	88.0	97.7	95.3	99.0
Integrated patterns (including multiple lattices)	58984	51812	27581	25464
Space group	<i>P</i> ₄ ₃ ₂ ₁ ₂	<i>P</i> ₄ ₃ ₂ ₁ ₂	<i>H</i> 3	<i>H</i> 3
Unit-cell parameters				
<i>a</i> = <i>b</i> (Å), <i>c</i> (Å)	79.0, 37.9	78.9, 37.9	177.9, 117.3	180.3, 119.2
α , β , γ (°)	90, 90, 90	90, 90, 90	90, 90, 120	90, 90, 120
Resolution (Å)	79.00–1.80 (1.83–1.80)	78.90–1.80 (1.83–1.80)	93.33–2.50 (2.54–2.50)	94.75–2.50 (2.54–2.50)
Total reflections	5096019 (26983)	5385630 (28772)	4534670 (215526)	4424291 (210986)
Unique reflections	11636 (669)	11607 (663)	47878 (4703)	50011 (4635)
Completeness (%)	100.0 (100.0)	100.0 (100.0)	100.0 (100.0)	100.0 (100.0)
Multiplicity	438.0 (47.67)	464.0 (51.94)	47.4 (45.18)	44.2 (41.83)
$\langle I/\sigma(I) \rangle$	13.5 (0.2)	17.2 (0.9)	4.4 (0.5)	5.0 (0.8)
CC _{1/2}	0.99 (0.49)	0.99 (0.44)	0.96 (0.17)	0.96 (0.27)
CC*	0.99 (0.81)	0.99 (0.78)	0.99 (0.54)	0.99 (0.65)
<i>R</i> _{split}	5.2 (343.7)	4.9 (100.8)	19.6 (212.2)	17.1 (147.3)
Wilson <i>B</i> -factor (Å ²)	30.5	24.1	49.4	45.3
Refinement				
PDB entry	8S2U	8S2V	8S2W	8S2X
Resolution (Å)	55.92–1.80	55.85–1.80	64.47–2.50	65.40–2.50
No. of reflections	11597	11567	47873	50003
Reflections used for <i>R</i> _{free}	581	581	2316	2510
<i>R</i> _{work}	0.171	0.146	0.168	0.158
<i>R</i> _{free}	0.231	0.190	0.193	0.188
No. of atoms				
Protein	1023	1064	8081	8118
Ligand/ion	2	2	20	72
Water	59	66	181	186
Ramachandran favoured	127 (98%)	130 (98%)	1042 (98%)	1057 (99%)
Ramachandran allowed	2 (2%)	3 (2%)	25 (2%)	15 (1%)
Ramachandran outliers	0 (0%)	0 (0%)	0 (0%)	0 (0%)
Rama distribution <i>Z</i> -score†	−0.65 ± 0.70	−0.29 ± 0.68	−1.87 ± 0.22	−1.17 ± 0.23
Clashscore†	0.99	1.43	4.17	2.00
<i>MolProbity</i> score†	0.79	1.20	1.27	0.97
R.m.s deviations				
Bond lengths (Å)	0.0066	0.0080	0.0054	0.0062
Bond angles (°)	1.551	1.767	1.407	1.511

† As determined by *MolProbity* (Williams *et al.*, 2018).

lower microcrystal concentration of 10⁷ ml^{−1} and its lower symmetry *H*3 space group.

We used a similar number of integrated lattices to compare data quality and chose the same resolution cut-off (1.8 Å for lysozyme and 2.5 Å for Pdx1). Data between batch and droplet crystallization are equivalent for CC_{1/2} and CC* indices, whilst gains in $\langle I/\sigma(I) \rangle$ and *R*_{split} are observed for crystals grown in droplets [Table 1 and Fig. S3]. Refinement statistics showed that the *R*_{free} was, in both cases, lower for crystals grown from droplets, compared with batch; however, the difference is higher for lysozyme (0.04) compared with Pdx1 (0.005). We note that the signal-to-noise ratio in the highest-resolution shell was higher for crystals grown in droplets, compared with batch, which follows the trend in Wilson *B* for the data collected. For the two samples we tested, these observations suggest that droplet-grown crystals were more ordered than batch-grown samples, likely due to limited convection in the microscopic droplet environment, with

diffusion being the dominant mode of transporting protein to the growing crystal, resulting in slower crystal growth.

3.5.1. Mixing in droplets. Substrate-triggered time-resolved experiments require the mixing of crystal and substrate volumes. The median *k*_{cat} for enzymes is 13.7 s^{−1} (~70 ms reaction cycles) (Bar-Even *et al.*, 2011), requiring mixing and into-crystal transport (and binding) times of a few milliseconds to synchronize reactions and allow intermediates to be effectively resolved. However, mixing in conventional microfluidic systems is slow, limited by substrate diffusion into the crystal stream. In contrast, microfluidic droplets lend themselves to fast mixing (Song & Ismagilov, 2003). Here, the transport of droplets in microchannels introduces circulations within the droplet for rapid, convective-diffusive mixing (Fig. S7). We went on to explore the merits of two different droplet-based mixing approaches.

3.5.2. Mixing by droplet generation and transport. The first system involves mixing by droplet generation and transport.

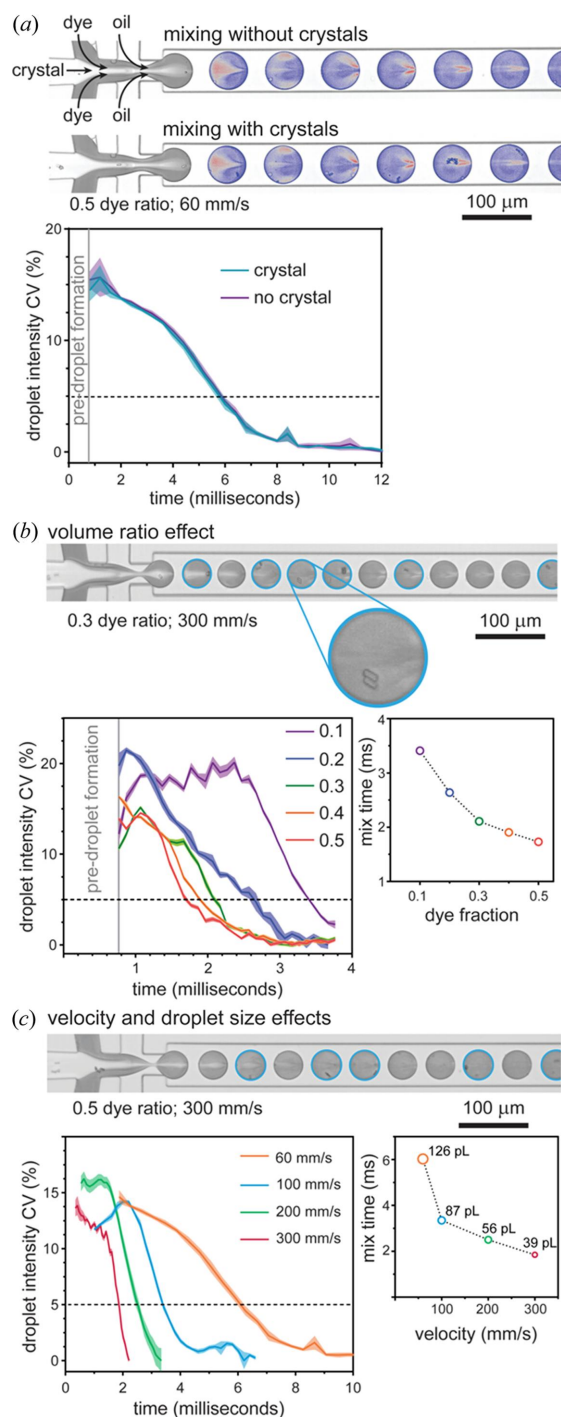


Figure 3 Mixing lysozyme crystals in droplets. (a) High-speed microscopy frame of mixing during droplet generation and transport along the channel (droplets are colour-enhanced to aid observation of mixing). The mixing rates with and without crystals are the same. Analysis involved 12 droplets with crystals and 10 droplets without. (b) Dye and crystal mixing in droplets at a ratio of 0.3 with a droplet velocity of 300 mm s^{-1} . Droplets containing crystals are highlighted with cyan circles. The mixing rate increases as the volume fraction of dye increases, with the optimal ratio being 0.5 (300 mm s^{-1} droplet velocity). The droplet pixel intensity CV is plotted as the mean \pm SD for 15 droplets. (c) Dye and crystal mixing in droplets at the optimal 0.5 ratio with a droplet velocity of 300 mm s^{-1} . The droplet pixel intensity CV is plotted as the mean \pm SD for 15 droplets. Increasing velocity increases convection (circulations within droplets) and shrinks droplet volumes to reduce diffusion paths, with both causing faster mixing.

Experiments involved the droplet encapsulation of a stream of pre-formed $\sim 7 \times 2 \mu\text{m}$ lysozyme crystals ($\sim 10^7 \text{ ml}^{-1}$) with a stream of red dye (SAA, 570 Da), comparable to a typical small-molecule substrate. Image analysis reveals that crystal and dye mixing during droplet generation occurs in a stepwise fashion: first, laminar streams converge with diffusion between streams initiating slow mixing, then droplet generation causes stream thinning (with short diffusion paths) for rapid mixing, followed by droplet transport with internal circulations driving mixing to completion [Fig. 3(a)]. Mixing begins upon flow convergence, with full mixing defined by a pixel intensity CV of 5%.

The presence of crystals within droplets did not affect mixing [Fig. 3(a)]. We next tested the ‘entropy of mixing’ theory (Ott & Boerio-Goates, 2000), which states that mixing is maximized when the volumes of initially separate liquids are equal. Indeed, at the same droplet velocity (300 mm s^{-1}), mixing times are reduced from 3.4 to 1.73 ms as the volume fraction of dye increases from 0.1 to 0.5 [Fig. 3(b)]. Taking this further, we investigated the effect of droplet velocity on mixing using the optimal 1:1 crystal:dye ratio. Increasing the velocity from 60 to 300 mm s^{-1} (droplet generation velocity limit) increased circulation speeds within droplets. Higher velocities also impart higher shear stresses during droplet generation, decreasing the droplet volume from 126 to 39 pL and producing shorter diffusion paths. Consequently, mixing times decrease from 6.0 ms at 60 mm s^{-1} to 1.85 ms at 300 mm s^{-1} [Fig. 3(c)], with faster mixing times anticipated using smaller and higher velocity droplets. Although mixing times are seldom reported, such fast mixing is equivalent to high-velocity co-axial capillary mixers (Calvey *et al.*, 2016), and exceeds mixing by drop-on-drop dispensing (Butryn *et al.*, 2021), or the $\sim 20 \text{ ms}$ mixing times reported for 3D-printed GDVN devices incorporating mixing blades (Knoška *et al.*, 2020).

3.5.3. Mixing initiated by droplet fusion. The ability to produce crystals in droplets affords an alternative strategy for mixing; protein crystals can be prepared in droplets by incubation (*e.g.* overnight) with droplets subsequently injected into a droplet device for fusion with substrate-containing droplets. This removes the need for breaking the emulsion, and moreover droplet-containment prevents crystal sedimentation within the syringe and channels being clogged. As a proof of principle, we developed a microfluidic circuit for generating 225 pL substrate droplets and synchronizing these with pre-formed 200 pL droplets containing crystals (Video S2). Synchronized droplet coupling was achieved by exploiting the size-dependent velocity differences between crystal-containing and substrate-containing droplets: the smaller, faster droplets approach and contact the larger droplets in readiness for fusion. A surfactant-exchange method was used for fusing droplets and initiating mixing (Mazutis *et al.*, 2009). Unlike mixing by droplet generation, this does not include the stream thinning effect for shortening diffusion paths. Reliable droplet fusion occurs at 100 mm s^{-1} , achieving mixing in $\sim 7 \text{ ms}$ (Video S3). Again, faster mixing is anticipated for smaller droplets. Note that into-crystal substrate transport can

occur earlier since convection within the droplet mobilizes the crystal throughout substrate-occupied regions before complete mixing is achieved. Nevertheless, the mixing times we report provide a conservative guide for the millisecond timescales that can be accessed, with the limiting step now being the into-crystal travel timescales of the substrate.

3.5.4. Droplets interfacing with the beam. To perform time-resolved experiments, mixing is followed by defined incubations and then crystal interaction with the beam. Importantly, droplets, and crystals within them, have the same transport velocity ensuring uniform incubation times. In contrast, conventional microfluidic transport suffers the effects of the parabolic velocity profile in which crystals in different streamlines are transported at different velocities (*i.e.* have different incubations). Periodic droplet generation with tuneable frequency (*e.g.* ~ 300 Hz to ~ 6 kHz in our reported mixing experiments) further offers potential for synchronization with beam repetition frequency to improve the hit rate. In practice, however, retaining periodicity during ejection into the beam introduces technical challenges which currently limit their potential (Echelmeier *et al.*, 2019, 2020; Doppler *et al.*, 2022; Sonker *et al.*, 2022). Droplet methods still exceed hit rates achieved using conventional GDVN methods, but now offer the benefits of faster micromixing for synchronized reaction triggering.

As an alternative to GDVN crystal injection into the beam, data collection can be achieved from within the microfluidic device, so-called *in situ* X-ray crystallography. Although PDMS is incompatible with X-rays due to high attenuation, it can nevertheless be used to analyse proteins with a spectral read-out. This enables experiment work-up in advance of visiting synchrotron or XFEL facilities. To exploit synchrotron capabilities and have broad utility, new challenges and technical possibilities emerge such as the fabrication of droplet microfluidic devices using thin-film materials (*e.g.* cyclic olefin co-polymer) that do not appreciably attenuate the X-ray beam (Sui *et al.*, 2016; Liu *et al.*, 2023). For much higher energy XFEL sources, the challenge of controlled ejection into the beam remains.

4. Conclusions

We have demonstrated droplet confinement and miniaturization for controlling crystal size and uniformity. At low picolitre and femtolitre scales, nucleation becomes improbable and can be bypassed using a seeding strategy for producing crystals only a few micrometres in length. The method was demonstrated with lysozyme and Pdx1, with crystals grown in droplets producing equivalent (if not better) diffraction data quality to those produced under batch conditions. Picolitre-scale droplet microfluidics also enables rapid, millisecond-scale micromixing to increase the temporal resolution of time-resolved experiments. Droplet microfluidic mixers can, in the future, be fabricated using thin-film, X-ray transparent materials for synchrotron experiments or coupled with beam injection methods to extend the approach to XFEL experi-

ments. In summary, droplet microfluidics methods offer great promise for improving time-resolved crystallography.

5. Related literature

The following references are cited in the supporting information: Agirre *et al.* (2023); Barty *et al.* (2014); Berman *et al.* (2003); Emsley *et al.* (2010); Gevorkov *et al.* (2019); Joosten *et al.* (2014); Monteiro *et al.* (2019); Murshudov *et al.* (2011); Potterton *et al.* (2018); Vagin & Teplyakov (2010); White (2019); White *et al.* (2012); Yefanov *et al.* (2015).

Acknowledgements

We thank Chris Holes for support with protein crystallization, ESRF for access to ID29 (under proposal Nos. MX2438 and MX2548) and Emma Beale for the adapted lysozyme crystallization conditions.

Funding information

The research was funded by a Diamond Doctoral Studentship Programme (studentship awarded to JS and RB); a South Coast Biosciences Doctoral Training Partnership (SoCoBio DTP) by the Biotechnology and Biological Sciences Research Council (BBSRC) (studentship No. BB/T008768/1 awarded to JS); BBSRC (studentship No. BB/S008470/1 awarded to IT); Science and Technology Facilities Council, Serial Data Processing and Analysis in CCP4i2 (awarded to IT and MM); Wellcome Investigator Award (award No. 210734/Z/18/Z awarded to AO); Royal Society Wolfson Fellowship (award No. RSWFR2 awarded to AO); NH acknowledges support from Engineering and Physical Sciences Research Council Impact Acceleration Account, EPSRC Transformative Healthcare Grant (grant No. EP/T020997/1), and University of Southampton Seed Enterprise Development Fund; University of Southampton Seed Enterprise Development Fund (awarded to NH).

References

- Agirre, J., Atanasova, M., Bagdonas, H., Ballard, C. B., Baslé, A., Beilstein-Edmands, J., Borges, R. J., Brown, D. G., Burgos-Mármol, J. J., Berrisford, J. M., Bond, P. S., Caballero, I., Catapano, L., Chojnowski, G., Cook, A. G., Cowtan, K. D., Croll, T. I., Debreczeni, J. É., Devenish, N. E., Dodson, E. J., Drevon, T. R., Emsley, P., Evans, G., Evans, P. R., Fando, M., Foadi, J., Fuentes-Montero, L., Garman, E. F., Gerstel, M., Gildea, R. J., Hatti, K., Hekkelman, M. L., Heuser, P., Hoh, S. W., Hough, M. A., Jenkins, H. T., Jiménez, E., Joosten, R. P., Keegan, R. M., Keep, N., Krissinel, E. B., Kolenko, P., Kovalevskiy, O., Lamzin, V. S., Lawson, D. M., Lebedev, A. A., Leslie, A. G. W., Lohkamp, B., Long, F., Malý, M., McCoy, A. J., McNicholas, S. J., Medina, A., Millán, C., Murray, J. W., Murshudov, G. N., Nicholls, R. A., Noble, M. E. M., Oeffner, R., Pannu, N. S., Parkhurst, J. M., Pearce, N., Pereira, J., Perrakis, A., Powell, H. R., Read, R. J., Rigden, D. J., Rochira, W., Sammito, M., Sánchez Rodríguez, F., Sheldrick, G. M., Shelley, K. L., Simkovic, F., Simpkin, A. J., Skubak, P., Sobolev, E., Steiner, R. A., Stevenson, K., Tews, I., Thomas, J. M. H., Thorn, A., Valls, J. T., Uski, V., Usón, I., Vagin, A., Velankar, S., Vollmar, M., Walden, H., Waterman, D.,

- Wilson, K. S., Winn, M. D., Winter, G., Wojdyr, M. & Yamashita, K. (2023). *Acta Cryst.* **D79**, 449–461.
- Akella, S. V., Mowitz, A., Heymann, M. & Fraden, S. (2014). *Cryst. Growth Des.* **14**, 4487–4509.
- Babnigg, G., Sherrell, D., Kim, Y., Johnson, J. L., Nocek, B., Tan, K., Axford, D., Li, H., Bigelow, L., Welk, L., Endres, M., Owen, R. L. & Joachimiak, A. (2022). *Acta Cryst.* **D78**, 997–1009.
- Barends, T. R. M., Stauch, B., Cherezov, V. & Schlichting, I. (2022). *Nat. Rev. Methods Primers*, **2**, 1–24.
- Bar-Even, A., Noor, E., Savir, Y., Liebermeister, W., Davidi, D., Tawfik, D. S. & Milo, R. (2011). *Biochemistry*, **50**, 4402–4410.
- Barty, A., Kirian, R. A., Maia, F. R. N. C., Hantke, M., Yoon, C. H., White, T. A. & Chapman, H. (2014). *J. Appl. Cryst.* **47**, 1118–1131.
- Beale, J. H., Bolton, R., Marshall, S. A., Beale, E. V., Carr, S. B., Ebrahim, A., Moreno-Chicano, T., Hough, M. A., Scholfield, J. A. R., Tews, I. & Owen, R. L. (2019). *J. Appl. Cryst.* **52**, 1385–1396.
- Beale, J. H. & Marsh, M. E. (2021). *JoVE J.* e61896.
- Berman, H., Henrick, K. & Nakamura, H. (2003). *Nat. Struct. Mol. Biol.* **10**, 980–980.
- Bücker, R., Hogan-Lamarre, P., Mehrabi, P., Schulz, E. C., Bultema, L. A., Gevorkov, Y., Brehm, W., Yefanov, O., Oberthür, D., Kassier, G. H. & Dwayne Miller, R. J. (2020). *Nat. Commun.* **11**, 996.
- Butryn, A., Simon, P. S., Aller, P., Hinchliffe, P., Massad, R. N., Leen, G., Tooke, C. L., Bogacz, I., Kim, I.-S., Bhowmick, A., Brewster, A. S., Devenish, N. E., Brem, J., Kamps, J. J. A. G., Lang, P. A., Rabe, P., Axford, D., Beale, J. H., Davy, B., Ebrahim, A., Orlans, J., Storm, S. L. S., Zhou, T., Owada, S., Tanaka, R., Tono, K., Evans, G., Owen, R. L., Houle, F. A., Sauter, N. K., Schofield, C. J., Spencer, J., Yachandra, V. K., Yano, J., Kern, J. F. & Orville, A. M. (2021). *Nat. Commun.* **12**, 4461.
- Calvey, G. D., Katz, A. M., Schaffer, C. B. & Pollack, L. (2016). *Struct. Dyn.* **3**, 054301.
- Carrillo, M., Mason, T., Karpik, A., Martiel, I., Kepa, M., McAuley, K., Beale, J. & Padeste, C. (2023). *IUCrJ*, **10**, 678–693.
- Chapman, H. N. (2019). *Annu. Rev. Biochem.* **88**, 35–58.
- Chapman, H. N., Fromme, P., Barty, A., White, T. A., Kirian, R. A., Aquila, A., Hunter, M. S., Schulz, J., DePonte, D. P., Weierstall, U., Doak, R. B., Maia, F. R. N. C., Martin, A. V., Schlichting, I., Lomb, L., Coppola, N., Shoeman, R. L., Epp, S. W., Hartmann, R., Rolles, D., Rudenko, A., Foucar, L., Kimmel, N., Weidenspointner, G., Holl, P., Liang, M., Barthelmeß, M., Caleman, C., Boutet, S., Bogan, M. J., Krzywinski, J., Bostedt, C., Bajt, S., Gumprecht, L., Rudek, B., Erk, B., Schmidt, C., Hömke, A., Reich, C., Pietschner, D., Strüder, L., Hauser, G., Gorke, H., Ullrich, J., Herrmann, S., Schaller, G., Schopper, F., Soltau, H., Kühnel, K. U., Messerschmidt, M., Bozek, J. D., Hau-Riege, S. P., Frank, M., Hampton, C. Y., Sierra, R. G., Starodub, D., Williams, G. J., Hajdu, J., Timneanu, N., Seibert, M. M., Andreasson, J., Røcker, A., Jönsson, O., Svenda, M., Stern, S., Nass, K., Andrichke, R., Schröter, C. D., Krasniqi, F., Bott, M., Schmidt, K. E., Wang, X., Grotjohann, I., Holton, J. M., Barends, T. R. M., Neutze, R., Marchesini, S., Fromme, R., Schorb, S., Rupp, D., Adolph, M., Gorkhover, T., Andersson, I., Hirsemann, H., Potdevin, G., Graafsma, H., Nilsson, B. & Spence, J. C. H. (2011). *Nature*, **470**, 73–77.
- D’Arcy, A., Villard, F. & Marsh, M. (2007). *Acta Cryst.* **D63**, 550–554.
- Dasgupta, M., Budday, D., de Oliveira, S. H. P., Madzlan, P., Marchany-Rivera, D., Seravalli, J., Hayes, B., Sierra, R. G., Boutet, S., Hunter, M. S., Alonso-Mori, R., Batyuk, A., Wierman, J., Lyubimov, A., Brewster, A. S., Sauter, N. K., Applegate, G. A., Tiwari, V. K., Berkowitz, D. B., Thompson, M. C., Cohen, A. E., Fraser, J. S., Wall, M. E., van den Bedem, H. & Wilson, M. A. (2019). *Proc. Natl Acad. Sci. USA*, **116**, 25634–25640.
- Davy, B., Axford, D., Beale, J. H., Butryn, A., Docker, P., Ebrahim, A., Leen, G., Orville, A. M., Owen, R. L. & Aller, P. (2019). *J. Synchrotron Rad.* **26**, 1820–1825.
- DePonte, D. P., Weierstall, U., Schmidt, K., Warner, J., Starodub, D., Spence, J. C. H. & Doak, R. B. (2008). *J. Phys. D Appl. Phys.* **41**, 195505.
- Doak, R. B., Nass Kovacs, G., Gorel, A., Foucar, L., Barends, T. R. M., Grünbein, M. L., Hilpert, M., Kloos, M., Roome, C. M., Shoeman, R. L., Stricker, M., Tono, K., You, D., Ueda, K., Sherrell, D. A., Owen, R. L. & Schlichting, I. (2018). *Acta Cryst.* **D74**, 1000–1007.
- Dombrowski, R. D., Litster, J. D., Wagner, N. J. & He, Y. (2007). *Chem. Eng. Sci.* **62**, 4802–4810.
- Doppler, D., Rabbani, M. T., Letrun, R., Cruz Villarreal, J., Kim, D. H., Gandhi, S., Egatz-Gomez, A., Sonker, M., Chen, J., Koua, F. H. M., Yang, J., Youssef, M., Mazalova, V., Bajt, S., Shelby, M. L., Coleman, M. A., Wiedorn, M. O., Knoska, J., Schön, S., Sato, T., Hunter, M. S., Hosseinizadeh, A., Kuptiz, C., Nazari, R., Alvarez, R. C., Karpos, K., Zaare, S., Dobson, Z., Discianno, E., Zhang, S., Zook, J. D., Bielecki, J., de Wijn, R., Round, A. R., Vagovic, P., Kloos, M., Vakili, M., Ketawala, G. K., Stander, N. E., Olson, T. L., Morin, K., Mondal, J., Nguyen, J., Meza-Aguilar, J. D., Kodis, G., Vaiana, S., Martin-Garcia, J. M., Mariani, V., Schwander, P., Schmidt, M., Messerschmidt, M., Ourmazd, A., Zatsepin, N., Weierstall, U., Bruce, B. D., Mancuso, A. P., Grant, T., Barty, A., Chapman, H. N., Frank, M., Fromme, R., Spence, J. C. H., Botha, S., Fromme, P., Kirian, R. A. & Ros, A. (2022). *J. Appl. Cryst.* **55**, 1–13.
- Echelmeier, A., Cruz Villarreal, J., Messerschmidt, M., Kim, D., Coe, J. D., Thifault, D., Botha, S., Egatz-Gomez, A., Gandhi, S., Brehm, G., Conrad, C. E., Hansen, D. T., Madsen, C., Bajt, S., Meza-Aguilar, J. D., Oberthür, D., Wiedorn, M. O., Fleckenstein, H., Mendez, D., Knoška, J., Martin-Garcia, J. M., Hu, H., Lisova, S., Allahgholi, A., Gevorkov, Y., Ayyer, K., Aplin, S., Ginn, H. M., Graafsma, H., Morgan, A. J., Greiffenberg, D., Klugev, A., Laurus, T., Poehls, J., Trunk, U., Mezza, D., Schmidt, B., Kuhn, M., Fromme, R., Sztuk-Dambietz, J., Raab, N., Hauf, S., Silenzi, A., Michelat, T., Xu, C., Danilevski, C., Parenti, A., Mekinda, L., Weinhausen, B., Mills, G., Vagovic, P., Kim, Y., Kirkwood, H., Bean, R., Bielecki, J., Stern, S., Giewekemeyer, K., Round, A. R., Schulz, J., Dörner, K., Grant, T. D., Mariani, V., Barty, A., Mancuso, A. P., Weierstall, U., Spence, J. C. H., Chapman, H. N., Zatsepin, N., Fromme, P., Kirian, R. A. & Ros, A. (2020). *Nat. Commun.* **11**, 4511.
- Echelmeier, A., Sonker, M. & Ros, A. (2019). *Anal. Bioanal. Chem.* **411**, 6535–6547.
- Emsley, P., Lohkamp, B., Scott, W. G. & Cowtan, K. (2010). *Acta Cryst.* **D66**, 486–501.
- Evans, G., Axford, D. & Owen, R. L. (2011). *Acta Cryst.* **D67**, 261–270.
- Fischer, M. (2021). *Q. Rev. Biophys.* **54**, e1.
- Förster, A., Brandstetter, S. & Schulze-Bries, C. (2019). *Phil. Trans. R. Soc. A*, **377**, 20180241.
- Forsythe, E. L. H., Snell, E., Malone, C. C. & Pusey, M. L. (1999). *J. Cryst. Growth*, **196**, 332–343.
- Fraser, J. S., van den Bedem, H., Samelson, A. J., Lang, P. T., Holton, J. M., Echols, N. & Alber, T. (2011). *Proc. Natl Acad. Sci. USA*, **108**, 16247–16252.
- Fuller, F. D., Gul, S., Chatterjee, R., Burgie, E. S., Young, I. D., Lebrete, H., Srinivas, V., Brewster, A. S., Michels-Clark, T., Clinger, J. A., Andi, B., Ibrahim, M., Pastor, E., de Lichtenberg, C., Hussein, R., Pollock, C. J., Zhang, M., Stan, C. A., Kroll, T., Fransson, T., Weninger, C., Kubin, M., Aller, P., Lassalle, L., Bräuer, P., Miller, M. D., Amin, M., Koroidov, S., Roessler, C. G., Allaire, M., Sierra, R. G., Docker, P. T., Glowina, J. M., Nelson, S., Koglin, J. E., Zhu, D., Chollet, M., Song, S., Lemke, H., Liang, M., Sokaras, D., Alonso-Mori, R., Zouni, A., Messinger, J., Bergmann, U., Boal, A. K., Bollinger, J. M., Krebs, C., Högbom, M., Phillips, G. N., Vierstra, R. D., Sauter, N. K., Orville, A. M., Kern, J., Yachandra, V. K. & Yano, J. (2017). *Nat. Methods*, **14**, 443–449.
- Garman, E. F. (2010). *Acta Cryst.* **D66**, 339–351.
- Garman, E. F. & Weik, M. (2023). *Curr. Opin. Struct. Biol.* **82**, 102662.
- Gati, C., Oberthuer, D., Yefanov, O., Bunker, R. D., Stellato, F., Chiu, E., Yeh, S.-M., Aquila, A., Basu, S., Bean, R., Beyerlein, K. R., Botha, S., Boutet, S., DePonte, D. P., Doak, R. B., Fromme, R., Galli, L., Grotjohann, I., James, D. R., Kupitz, C., Lomb, L., Messerschmidt, M., Nass, K., Rendek, K., Shoeman, R. L., Wang,

- D., Weierstall, U., White, T. A., Williams, G. J., Zatsepin, N. A., Fromme, P., Spence, J. C. H., Goldie, K. N., Jehle, J. A., Metcalf, P., Barty, A. & Chapman, H. N. (2017). *Proc. Natl Acad. Sci. USA*, **114**, 2247–2252.
- Gevorkov, Y., Yefanov, O., Barty, A., White, T. A., Mariani, V., Brehm, W., Tolstikova, A., Grigat, R.-R. & Chapman, H. N. (2019). *Acta Cryst. A* **75**, 694–704.
- Hansen, C. L., Skordalakes, E., Berger, J. M. & Quake, S. R. (2002). *Proc. Natl Acad. Sci. USA*, **99**, 16531–16536.
- Heymann, M., Ophthalage, A., Wierman, J. L., Akella, S., Szebenyi, D. M. E., Gruner, S. M. & Fraden, S. (2014). *IUCrJ*, **1**, 349–360.
- Holton, J. M. (2009). *J. Synchrotron Rad.* **16**, 133–142.
- Hunter, M. S., Segelke, B., Messerschmidt, M., Williams, G. J., Zatsepin, N. A., Barty, A., Benner, W. H., Carlson, D. B., Coleman, M., Graf, A., Hau-Riege, S. P., Pardini, T., Seibert, M. M., Evans, J., Boutet, S. & Frank, M. (2014). *Sci. Rep.* **4**, 6026.
- Ishigami, I., Lewis-Ballester, A., Echelmeier, A., Brehm, G., Zatsepin, N. A., Grant, T. D., Coe, J. D., Lisova, S., Nelson, G., Zhang, S., Dobson, Z. F., Boutet, S., Sierra, R. G., Batyuk, A., Fromme, P., Fromme, R., Spence, J. C. H., Ros, A., Yeh, S.-R. & Rousseau, D. L. (2019). *Proc. Natl Acad. Sci. USA*, **116**, 3572–3577.
- Joosten, R. P., Long, F., Murshudov, G. N. & Perrakis, A. (2014). *IUCrJ*, **1**, 213–220.
- Knoška, J., Adriano, L., Awel, S., Beyerlein, K. R., Yefanov, O., Oberthuer, D., Peña Murillo, G. E., Roth, N., Sarrou, I., Villanueva-Perez, P., Wiedorn, M. O., Wilde, F., Bajt, S., Chapman, H. N. & Heymann, M. (2020). *Nat. Commun.* **11**, 657.
- Lane, S. I. R., Butement, J., Harrington, J., Underwood, T., Shrimpton, J. & West, J. (2019). *Lab Chip*, **19**, 3771–3775.
- Li, L. & Ismagilov, R. F. (2010). *Annu. Rev. Biophys.* **39**, 139–158.
- Liu, Z., Gu, K. K., Shelby, M. L., Gilbille, D., Lyubimov, A. Y., Russi, S., Cohen, A. E., Narayanasamy, S. R., Botha, S., Kupitz, C., Sierra, R. G., Poitevin, F., Gilardi, A., Lisova, S., Coleman, M. A., Frank, M. & Kuhl, T. L. (2023). *Acta Cryst. D* **79**, 944–952.
- Martin-Garcia, J. M., Conrad, C. E., Nelson, G., Stander, N., Zatsepin, N. A., Zook, J., Zhu, L., Geiger, J., Chun, E., Kissick, D., Hilgart, M. C., Ogata, C., Ishchenko, A., Nagaratnam, N., Roy-Chowdhury, S., Coe, J., Subramanian, G., Schaffer, A., James, D., Ketwala, G., Venugopalan, N., Xu, S., Corcoran, S., Ferguson, D., Weierstall, U., Spence, J. C. H., Cherezov, V., Fromme, P., Fischetti, R. F. & Liu, W. (2017). *IUCrJ*, **4**, 439–454.
- Mazutis, L., Baret, J. C. & Griffiths, A. D. (2009). *Lab Chip*, **9**, 2665–2672.
- Mehrabi, P., Müller-Werkmeister, H. M., Leimkohl, J.-P., Schikora, H., Ninkovic, J., Krivokuca, S., Andriček, L., Epp, S. W., Sherrell, D., Owen, R. L., Pearson, A. R., Tellkamp, F., Schulz, E. C. & Miller, R. J. D. (2020). *J. Synchrotron Rad.* **27**, 360–370.
- Mehrabi, P., Schulz, E. C., Agthe, M., Horrell, S., Bourenkov, G., von Stetten, D., Leimkohl, J.-P., Schikora, H., Schneider, T. R., Pearson, A. R., Tellkamp, F. & Miller, R. J. D. (2019). *Nat. Methods*, **16**, 979–982.
- Monteiro, D. C. F., Vakili, M., Harich, J., Sztucki, M., Meier, S. M., Horrell, S., Josts, I. & Trebbin, M. (2019). *J. Synchrotron Rad.* **26**, 406–412.
- Mozzanica, A., Andrä, M., Barten, R., Bergamaschi, A., Chiriotti, S., Brückner, M., Dinapoli, R., Fröjd, E., Greiffenberg, D., Leonarski, F., Lopez-Cuenca, C., Mezza, D., Redford, S., Ruder, C., Schmitt, B., Shi, X., Thattil, D., Tinti, G., Vetter, S. & Zhang, J. (2018). *Synchrotron Radiat. News*, **31**, 16–20.
- Murakawa, T., Suzuki, M., Fukui, K., Masuda, T., Sugahara, M., Tono, K., Tanaka, T., Iwata, S., Nango, E., Yano, T., Tanizawa, K. & Okajima, T. (2022). *Acta Cryst. D* **78**, 1428–1438.
- Murshudov, G. N., Skubák, P., Lebedev, A. A., Pannu, N. S., Steiner, R. A., Nicholls, R. A., Winn, M. D., Long, F. & Vagin, A. A. (2011). *Acta Cryst. D* **67**, 355–367.
- Olmos, J. L., Pandey, S., Martin-Garcia, J. M., Calvey, G., Katz, A., Knoška, J., Kupitz, C., Hunter, M. S., Liang, M., Oberthuer, D., Yefanov, O., Wiedorn, M., Heyman, M., Holl, M., Pande, K., Barty, A., Miller, M. D., Stern, S., Roy-Chowdhury, S., Coe, J., Nagaratnam, N., Zook, J., Verburg, J., Norwood, T., Poudyal, I., Xu, D., Koglin, J., Seaberg, M. H., Zhao, Y., Bajt, S., Grant, T., Mariani, V., Nelson, G., Subramanian, G., Bae, E., Fromme, R., Fung, R., Schwander, P., Frank, M., White, T. A., Weierstall, U., Zatsepin, N., Spence, J., Fromme, P., Chapman, H. N., Pollack, L., Tremblay, L., Ourmazd, A., Phillips, G. N. & Schmidt, M. (2018). *BMC Biol.* **16**, 59.
- Orville, A. M. (2020). *Curr. Opin. Struct. Biol.* **65**, 193–208.
- Ott, J. B. & Boerio-Goates, J. (2000). *Chemical Thermodynamics: Principles and Applications*. Academic Press.
- Owen, R. L., Axford, D., Sherrell, D. A., Kuo, A., Ernst, O. P., Schulz, E. C., Miller, R. J. D. & Mueller-Werkmeister, H. M. (2017). *Acta Cryst. D* **73**, 373–378.
- Pandey, S., Calvey, G., Katz, A. M., Malla, T. N., Koua, F. H. M., Martin-Garcia, J. M., Poudyal, I., Yang, J.-H., Vakili, M., Yefanov, O., Zielinski, K. A., Bajt, S., Awel, S., Doerner, K., Frank, M., Gelisio, L., Jernigan, R., Kirkwood, H., Kloos, M., Koliyadu, J., Mariani, V., Miller, M. D., Mills, G., Nelson, G., Olmos, J. L., Sadri, A., Sato, T., Tolstikova, A., Xu, W., Ourmazd, A., Spence, J. H. C., Schwander, P., Barty, A., Chapman, H. N., Fromme, P., Mancuso, A. P., Phillips, G. N., Bean, R., Pollack, L. & Schmidt, M. (2021). *IUCrJ*, **8**, 878–895.
- Potterton, L., Agirre, J., Ballard, C., Cowtan, K., Dodson, E., Evans, P. R., Jenkins, H. T., Keegan, R., Krissinel, E., Stevenson, K., Lebedev, A., McNicholas, S. J., Nicholls, R. A., Noble, M., Pannu, N. S., Roth, C., Sheldrick, G., Skubak, P., Turkenburg, J., Uski, V., von Delft, F., Waterman, D., Wilson, K., Winn, M. & Wojdyr, M. (2018). *Acta Cryst. D* **74**, 68–84.
- Puigmartí-Luis, J. (2014). *Chem. Soc. Rev.* **43**, 2253–2271.
- Rodrigues, M. J., Giri, N., Royant, A., Zhang, Y., Bolton, R., Evans, G., Ealick, S. E., Begley, T. & Tews, I. (2022). *RSC Chem. Biol.* **3**(2), 227–230.
- Rodrigues, M. J., Windeisen, V., Zhang, Y., Guédez, G., Weber, S., Strohmeier, M., Hanes, J. W., Royant, A., Evans, G., Sinning, I., Ealick, S. E., Begley, T. P. & Tews, I. (2017). *Nat. Chem. Biol.* **13**, 290–294.
- Roedig, P., Vartiainen, I., Duman, R., Panneerselvam, S., Stübe, N., Lorbeer, O., Warmer, M., Sutton, G., Stuart, D. I., Weckert, E., David, C., Wagner, A. & Meents, A. (2015). *Sci. Rep.* **5**, 10451.
- Roessler, C. G., Agarwal, R., Allaire, M., Alonso-Mori, R., Andi, B., Bachega, J. F. R., Bommer, M., Brewster, A. S., Browne, M. C., Chatterjee, R., Cho, E., Cohen, A. E., Cowan, M., Datwani, S., Davidson, V. L., Defever, J., Eaton, B., Ellison, R., Feng, Y., Ghislain, L. P., Glowina, J. M., Han, G., Hattne, J., Hellmich, J., Héroux, A., Ibrahim, M., Kern, J., Kuczewski, A., Lemke, H. T., Liu, P., Majlof, L., McClintock, W. M., Myers, S., Nelsen, S., Olechno, J., Orville, A. M., Sauter, N. K., Soares, A. S., Soltis, S. M., Song, H., Stearns, R. G., Tran, R., Tsai, Y., Uervirojnangkoon, M., Wilmot, C. M., Yachandra, V., Yano, J., Yukl, E. T., Zhu, D. & Zouni, A. (2016). *Structure*, **24**, 631–640.
- Schmidt, M. (2013). *Adv. Condens. Matter Phys.* **2013**, 167276.
- Schulz, E. C., Yorke, B. A., Pearson, A. R. & Mehrabi, P. (2022). *Acta Cryst. D* **78**, 14–29.
- Selimović, Š., Jia, Y. & Fraden, S. (2009). *Cryst. Growth Des.* **9**, 1806–1810.
- Shaw Stewart, P. D., Kolek, S. A., Briggs, R. A., Chayen, N. E. & Baldock, P. F. M. (2011). *Cryst. Growth Des.* **11**, 3432–3441.
- Shi, H., Xiao, Y., Ferguson, S., Huang, X., Wang, N. & Hao, H. (2017). *Lab Chip*, **17**, 2167–2185.
- Shim, J., Cristobal, G., Link, D. R., Thorsen, T. & Fraden, S. (2007a). *Cryst. Growth Des.* **7**, 2192–2194.
- Shim, J., Cristobal, G., Link, D. R., Thorsen, T., Jia, Y., Piattelli, K. & Fraden, S. (2007b). *J. Am. Chem. Soc.* **129**, 8825–8835.
- Shoeman, R. L., Hartmann, E. & Schlichting, I. (2022). *Nat. Protoc.* **18**, 854–882.
- Song, H. & Ismagilov, R. F. (2003). *J. Am. Chem. Soc.* **125**, 14613–14619.

- Sonker, M., Doppler, D., Egatz-Gomez, A., Zaare, S., Rabbani, M. T., Manna, A., Villarreal, J. C., Nelson, G., Ketawala, G. K., Karpos, K. & Alvarez, R. C. (2022). *Biophys. Rep.* **2**, 100081.
- Stagno, J. R., Liu, Y., Bhandari, Y. R., Conrad, C. E., Panja, S., Swain, M., Fan, L., Nelson, G., Li, C., Wendel, D. R., White, T. A., Coe, J. D., Wiedorn, M. O., Knoska, J., Oberthuer, D., Tuckey, R. A., Yu, P., Dyba, M., Tarasov, S. G., Weierstall, U., Grant, T. D., Schwieters, C. D., Zhang, J., Ferré-D'Amaré, A. R., Fromme, P., Draper, D. E., Liang, M., Hunter, M. S., Boutet, S., Tan, K., Zuo, X., Ji, X., Barty, A., Zatsépin, N. A., Chapman, H. N., Spence, J. C. H., Woodson, S. A. & Wang, Y.-X. (2017). *Nature*, **541**, 242–246.
- Stohrer, C., Horrell, S., Meier, S., Sans, M., von Stetten, D., Hough, M., Goldman, A., Monteiro, D. C. F. & Pearson, A. R. (2021). *Acta Cryst.* **D77**, 194–204.
- Stura, E. A. & Wilson, I. A. (1990). *Methods*, **1**, 38–49.
- Sui, S. & Perry, S. L. (2017). *Struct. Dyn.* **4**, 032202.
- Sui, S., Wang, Y., Kolewe, K. W., Srajer, V., Henning, R., Schiffman, J. D., Dimitrakopoulos, C. & Perry, S. L. (2016). *Lab Chip*, **16**, 3082–3096.
- Tenboer, J., Basu, S., Zatsépin, N., Pande, K., Milathianaki, D., Frank, M., Hunter, M., Boutet, S., Williams, G. J., Koglin, J. E., Oberthuer, D., Heymann, M., Kupitz, C., Conrad, C., Coe, J., Roy-Chowdhury, S., Weierstall, U., James, D., Wang, D., Grant, T., Barty, A., Yefanov, O., Scales, J., Gati, C., Seuring, C., Srajer, V., Henning, R., Schwander, P., Fromme, R., Ourmazd, A., Moffat, K., Van Thor, J. J., Spence, J. C. H., Fromme, P., Chapman, H. N. & Schmidt, M. (2014). *Science*, **346**, 1242–1246.
- Vagin, A. & Teplyakov, A. (2010). *Acta Cryst.* **D66**, 22–25.
- Weierstall, U., Spence, J. C. H. & Doak, R. B. (2012). *Rev. Sci. Instrum.* **83**, 035108.
- White, T. A. (2019). *Acta Cryst.* **D75**, 219–233.
- White, T. A., Kirian, R. A., Martin, A. V., Aquila, A., Nass, K., Barty, A. & Chapman, H. N. (2012). *J. Appl. Cryst.* **45**, 335–341.
- Whitesides, G. M. (2006). *Nature*, **442**, 368–373.
- Whitesides, G. M., Ostuni, E., Takayama, S., Jiang, X. & Ingber, D. E. (2001). *Annu. Rev. Biomed. Eng.* **3**, 335–373.
- Williams, C. J., Headd, J. J., Moriarty, N. W., Prisant, M. G., Videau, L. L., Deis, L. N., Verma, V., Keedy, D. A., Hintze, B. J., Chen, V. B., Jain, S., Lewis, S. M., Arendall, W. B. III, Snoeyink, J., Adams, P. D., Lovell, S. C., Richardson, J. S. & Richardson, D. C. (2018). *Protein Sci.* **27**, 293–315.
- Williamson, L. J., Galchenkova, M., Best, H. L., Bean, R. J., Munke, A., Awel, S., Pena, G., Knoska, J., Schubert, R., Dörner, K., Park, H.-W., Bideshi, D. K., Henkel, A., Kremling, V., Klopprogge, B., Lloyd-Evans, E., Young, M. T., Valerio, J., Kloos, M., Sikorski, M., Mills, G., Bielecki, J., Kirkwood, H., Kim, C., de Wijn, R., Lorenzen, K., Xavier, P. L., Rahmani Mashhour, A., Gelisio, L., Yefanov, O., Mancuso, A. P., Federici, B. A., Chapman, H. N., Crickmore, N., Rizkallah, P. J., Berry, C. & Oberthür, D. (2023). *Proc. Natl Acad. Sci. USA*, **120**, e2203241120.
- Yefanov, O., Mariani, V., Gati, C., White, T. A., Chapman, H. N. & Barty, A. (2015). *Opt. Express*, **23**, 28459–28470.
- Zheng, B., Tice, J. D., Roach, L. S. & Ismagilov, R. F. (2004). *Angew. Chem. Int. Ed.* **43**, 2508–2511.